TEMPORAL DOPPLER EFFECTS IN SAS

Dr David W. Hawkins[1], Professor Peter T. Gough[2]

[1]Owen's Valley Radio Observatory,
California Institute of Technology, Big Pine, CA 93514, USA.
dwh@ovro.caltech.edu

[2]Acoustics Research Group, Department of Electrical and Computer Engineering,
University of Canterbury, Private Bag 4800, Christchurch, New Zealand.
peter.gough@canterbury.ac.nz

1. INTRODUCTION

The Doppler effect refers to the apparent change in frequency of a signal due to relative source-observer motion. Although the Doppler effect is almost always described and defined in terms of a frequency effect, the actual effect corresponds to a time-domain compression or expansion.

In a SAS system, a tow platform contains a transmitter and a receiver, and observes targets off to the side of the tow path. SAS imaging models are typically developed under the 'stop-and-hop' model, whereby it is assumed that the platform transmits a signal, receives the echos from targets, and then jumps to the next along-track sampling location. This simplified model is adequate for systems towed at speeds of less than 1m/s with small pulse lengths (eg. less than say 50ms). However, temporal Doppler effects must be compensated for in systems employing long pulse lengths, or with high tow-speeds. High tow-speeds are now common with the advent of multiple along-track receiver SAS systems.

Treatment of temporal Doppler in the radar and sonar community originated in the context of narrow bandwidth active systems measuring the motion parameters (range, velocity, and acceleration) of moving targets. Narrow bandwidth systems model the Doppler effect not as a time-domain compression, but as a simple frequency shift. In SAS imaging, it is not the targets that are moving, but the sonar system. The motion of the platform during both transmission and reception causes the Doppler effect to occur in the measured echos. SAS imaging has the advantage that the platform-target relative speeds, and hence Doppler shifts are known, and can therefore be compensated.

Migrating from the standard 'stop-and-hop' SAS system model to a model that incorporates the effect of platform motion requires the compensation of two effects; a geometric distortion, and temporal Doppler distortion—the compression and expansion of the transmit signals and receive echos due to platform motion during transmission and reception. In the 'stop-and-hop' system model, the range from a SAS platform at along-track location u to a target located at (x, y) for pulse transmission *and* reception is

$$r = \sqrt{x^2 + (y - u)^2} \tag{1}$$

so a pulse transmitted at time t is received at time $t + \tau$ where

$$\tau = \frac{2r}{c}. \tag{2}$$

In reality, a sonar traveling at speed v will have traveled a distance $\sim v\tau$ by the time an echo from range r is received. The round-trip time for an echo transmitted at time t can be derived using the cosine rule [1] to give

$$\tau_v = \frac{2cr - 2v(y-u)}{c^2 - v^2} \tag{3}$$

where a pulse transmitted at time t is received at time $t + \tau_v$. This equation can be used to determine the platform-motion induced geometric distortion and Doppler distortion on a transmitted pulse. Reference [1] shows that the geometric distortion of a processed target is that its along-track location is skewed by half the distance moved by the platform for a target at that range. This geometric skew is independent of signal parameters and does not result in image defocus. Doppler distortion does result in image defocus, and is the subject of this paper.

2. TEMPORAL DOPPLER

Assume that the range between a source (moving with a closing velocity of $v_{\rm src}$) and an observer (with closing velocity $v_{\rm obs}$—both these velocities relative to the environment) can be described as

$$r(t) = r_0 - v_{\rm src}t - v_{\rm obs}t \tag{4}$$

where r_0 is the range at time $t = 0$. The "classical" definition for the temporal Doppler effect on a *single continuous frequency* is then given by

$$f_0' = \left(\frac{1 + v_{\rm obs}/c}{1 - v_{\rm src}/c}\right) \cdot f_0 \tag{5}$$

where f_0 is the transmitted frequency and f_0' is the received Doppler distorted frequency. As an example of how a single frequency can be Doppler shifted differing amounts, consider the following three scenarios. Given the speed of sound in air of $c = 340$m/s, and a relative source-platform velocity of $v = 20$m/s (72km/hr or 45mph), an $f_0 = 1$kHz sinusoid can be Doppler shifted according to three possible relative motion cases for the same decreasing source-observer distance;

1. Source at rest, observer moving at v; $f_0' = (1 + 20/340)1\text{kHz} = 1.0588\text{kHz}$.
2. Source moving at v, observer at rest; $f_0' = 1\text{kHz}/(1 - 20/340) = 1.0625\text{kHz}$.
3. Source moving at $v/2$, observer moving at $v/2$; $f_0' = 1\text{kHz}(1 + 10/340)/(1 - 10/340) = 1.0606\text{kHz}$.

2.1 The Doppler effect on a sonar waveform

For all active sonars, there are two parts to the acoustic path from the source to observer. The sound is radiated from the source, propagates through the medium, reflects off a target, propagates back through the same medium and is detected by an observer. In some situations,

the sonar platform (containing both the source and the observer) is stationary and the target moves and for others, the sonar moves and the target is stationary. For the moving sonar, the velocity of the source on the outward path is equal (linear platform-target motion), or approximately equal (SAS imaging), to the velocity of the observer on the return path. The single-frequency Doppler shift for the echo received by a moving sonar can be recast in terms a single velocity variable using the range rate $\dot{r}(t)$. Thus the following equation is appropriate for linear platform-target motion where either (i) there is common movement of the source and the receiver relative to a stationary target or (ii) the source and receiver are stationary and the target moves

$$f_0' = \left(\frac{1-\dot{r}(t)/c}{1+\dot{r}(t)/c}\right)\cdot f_0 \approx \left(1-\frac{2\dot{r}(t)}{c}\right)\cdot f_0 \tag{6}$$

where the approximation is valid for sonar since $\dot{r}(t) \ll c$. The Doppler effect in (6) is applicable to a narrow bandwidth signal of frequency f_0, and to the *carrier frequency*, f_0, of a wideband signal. The distortion of the other spectral components in a wideband signal is provided shortly.

Narrow bandwidth analysis of the Doppler effect for sonar imaging starts with (6) and defines it as

$$f_0' \approx f_0 + f_d \tag{7}$$

where the *Doppler frequency shift* is given by

$$f_d \approx -\frac{2\dot{r}(t)}{c} f_0. \tag{8}$$

The negative sign is defined as part of f_d so that for an observer approaching the target, the Doppler shift is *positive* since the range-rate is $-v$, and the observed frequency is higher. Conversely, for a receding observer, the range-rate is positive, so the Doppler shift is negative, and the observed frequency is lower. The seemingly logical sign convention for the Doppler shift is not uniformly used in the radar and sonar literature.

Given a narrow bandwidth transmit signal, $p(t)$, the received temporal Doppler shifted echo (ignoring the round-trip delay) is

$$e(t) \approx p(t)\exp(j2\pi f_d t) \tag{9}$$

with the echo spectrum given by

$$E(f) \approx P(f-f_d). \tag{10}$$

The target range (delay) and velocity (Doppler shift) are determined at the receiver by correlating the incoming signal against delayed and Doppler shifted versions of the transmitted pulse. The sensitivity of a signal to an incorrect delay or Dopper shift estimate is described by the narrowband (Woodward) ambiguity function (NAF) (p119 [2], [3])

$$\begin{aligned}\chi_n(\tau, f_d) &= \int p(t)p^*(t-\tau)\exp(j2\pi f_d t)dt \\ &= \int P(f-f_d)P^*(f)\exp(j2\pi f\tau)df\end{aligned} \tag{11}$$

(the delay parameter τ is centered on zero, but in application each target has an ambiguity function and τ represents the uncertainty in the target delay measurement). The magnitude of the ambiguity function, $|\chi_n(\tau, f_d)|$, is referred to as an ambiguity diagram. The ambiguity diagram peaks at $(\tau, f_d) = (0, 0)$ (no error in the parameter estimates), and typically has a linear ridge in delay-Doppler space before the peak drops. Rihaczek's classic radar text [2] contains examples of ambiguity diagrams, as does Mitchell and Rihaczek's paper [4], and the text by Cook and Bernfeld [5].

Wide bandwidth analysis of the Doppler effect for sonar imaging requires treating the effect as a time-domain scaling, i.e., the Doppler effect has the form

$$t' = t/\eta. \tag{12}$$

where the *Doppler scale-factor*, η, is often defined as

$$\eta \approx \left(\frac{1 - \dot{r}(t)/c}{1 + \dot{r}(t)/c}\right) \approx \left(1 - \frac{2\dot{r}(t)}{c}\right) \tag{13}$$

where this definition is approximate in that η is calculated as a constant value, using a range-rate calculated as a constant for each pulse transmission and echo reception, i.e., at each along-track location in the synthetic aperture, the range-rate and η are calculated for time equal to pulse transmission time, and considered constant, until the next pulse transmission.

Using the round-trip time in (3) the transmission of a pulse of length τ_p centered at time $t = 0$ can be used to determine the length of the received pulse and hence the Doppler scale-factor for the true motion case. The start of the transmitted pulse is transmitted at time $t = -\tau_p/2$ and arrives back at the receiver at time $-\tau_p/2 + \tau_v(-\tau_p/2)$, while the end of the transmitted pulse is transmitted at time $t = \tau_p/2$ and arrives back at the receiver at time $\tau_p/2 + \tau_v(\tau_p/2)$. The difference between the pulse edges at the receiver gives the length of the Doppler distorted pulse, i.e., $\tau'_p = \tau_v(\tau_p/2) - \tau_v(-\tau_p/2) + \tau_p = \tau_p/\eta$. Reference [1] contains the intermediate steps, with the resulting Doppler scale factor being

$$\eta_{\text{sas}}(t) = \frac{\tau_p}{\tau'_p} = \left(1 + \frac{2c\left(\sqrt{x^2 + (y - u - v\tau_p/2)^2} - \sqrt{x^2 + (y - u + v\tau_p/2)^2}\right) + 2v^2\tau_p}{\tau_p(c^2 - v^2)}\right)^{-1} \tag{14}$$

which using a quadratic expansion for the square-root terms can be approximated (linearized in t) as

$$\eta_{\text{sas}}(t) \approx 1 - \frac{2cv^2(t + x/c - y/v)}{x(c^2 - v^2)} \approx 1 - \frac{2v^2(t - y/v)}{cx} \tag{15}$$

where the last approximation can be also derived using a modified 'stop-and- hop' assumption [1]. In practice, the linearized equations are only valid for narrow beamwidths. For wide beamwidths, (14) should be used.

When analyzing the Doppler effect, it is useful to keep in mind the following (intuitive) expectation; a decreasing platform-target range results in a compression of the received echo pulse, and

higher frequencies in the spectrum, while a receding platform-target range results in a longer pulse, and lower frequencies in the spectrum.

Given a wideband transmit signal $p(t)$, the Doppler distorted echo $e(t)$ is derived by substitution, i.e., $t = \eta t'$ to give

$$e(t') = p(\eta t') \tag{16}$$

and once the substitution is complete, the prime on the time-scaled parameter is dropped, i.e.,

$$e(t) = p(\eta t) \tag{17}$$

which has the spectrum

$$E(f) = \frac{1}{\eta} P\left(\frac{f}{\eta}\right). \tag{18}$$

The wideband (Kelly and Wishner) ambiguity function is then [6–10]

$$\begin{aligned} \chi_w(\tau, \eta) &= \sqrt{\eta} \int p(\eta t) p^*(t - \tau) dt \\ &= \frac{1}{\sqrt{\eta}} \int P\left(\frac{f}{\eta}\right) P^*(f) \exp(j2\pi f \tau) df \end{aligned} \tag{19}$$

which as for the narrow band ambiguity function, can be interpreted as the correlation of the received Doppler distorted pulse with the transmitted pulse. The scale factor $\sqrt{\eta}$ normalizes the wideband ambiguity function. It is sometimes seen as part of the echo $e(t)$, introduced during the substitution to scaled-time to preserve energy [11].

2.2 Sinusoidal Pulse

To show the effects of Doppler distortion, we first consider the case of a platform traveling toward a target initially at a range r_0, at a speed v, that transmits a sinusoidal pulse of frequency f_0 and duration τ_p centered on time $t = 0$, i.e.,

$$p(t) = \text{rect}\left(\frac{t}{\tau_p}\right) \exp(j2\pi f_0 t) \quad \text{and} \quad P(f) = \tau_p \text{sinc}\left\{(f - f_0)\tau_p\right\}. \tag{20}$$

The received Doppler distorted pulse using (17) is

$$e(t) = \text{rect}\left(\frac{\eta t}{\tau_p}\right) \exp\left(j2\pi f_0 \eta t\right) = \text{rect}\left(\frac{t}{\tau_p'}\right) \exp(j2\pi f_0' t) \tag{21}$$

and using this equation

$$E(f) = \tau_p' \text{sinc}\left\{(f - f_0')\tau_p'\right\} = \frac{1}{\eta} \tau_p \text{sinc}\left\{\left(\frac{f}{\eta} - f_0\right)\tau_p\right\} \tag{22}$$

which is consistent with (18). Since the platform-target range is decreasing, the temporal domain is compressed, and the Doppler scale-factor $\eta > 1$, resulting in a shorter pulse $\tau_p' = \tau_p/\eta < \tau_p$, and a higher received sinusoid $f_0' = \eta f_0 > f_0$. Note that this wideband analysis gives the encouraging result that the Doppler shift of the sinusoid is identical to that predicted by the narrowband formulation.

2.3 Linear FM chirp

Now consider the case of the transmission of a linear FM (LFM) chirp of bandwidth B, duration τ_p centered on time $t = 0$. The modulated complex form of the LFM chirp is

$$p(t) = \text{ rect}\left(\frac{t}{\tau_p}\right) \cdot \exp\left\{j2\pi\left(f_0 t + \frac{1}{2}Kt^2\right)\right\} \tag{23}$$

which (for large time-bandwidth pulses) has the Fourier transform

$$P(f) \approx \text{ rect}\left(\frac{f - f_0}{B}\right) \cdot \sqrt{\frac{j}{K}} \cdot \exp\left(-j\pi\frac{(f - f_0)^2}{K}\right). \tag{24}$$

The Doppler distorted echo is

$$e(t) = p(\eta t) = \text{ rect}\left(\frac{\eta t}{\tau_p}\right) \cdot \exp\left\{j2\pi\left(f_0\eta t + \frac{1}{2}K\eta^2 t^2\right)\right\} \tag{25}$$

which (for large time-bandwidth pulses) has the Fourier transform

$$E(f) = \frac{1}{\eta} \cdot P\left(\frac{f}{\eta}\right) \approx \frac{1}{\eta} \cdot \text{ rect}\left(\frac{f - \eta f_0}{\eta B}\right) \cdot \sqrt{\frac{j}{K}} \cdot \exp\left(-j\pi\frac{(f - \eta f_0)^2}{\eta^2 K}\right). \tag{26}$$

Relative to the original chirp, the Doppler distorted chirp has a new pulse length $\tau_p' = \tau_p/\eta$, new carrier frequency $f_0' = \eta f_0$, new chirp rate $K' = \eta^2 K$, and new bandwidth $B' = \eta K \tau_p = \eta B$. Note that the Doppler shift of the carrier matches the Doppler shift predicted by narrowband theory, however, the narrowband analysis does not predict the distortion of frequencies away from the carrier.

Doppler distortion of LFM chirps results in a change in the received signal carrier and chirp rate. Pulse compression of the *received Doppler distorted chirps* using a phase reference based on the *transmitted chirp* results in the correlation of signals with different carriers and different chirp-rates. This correlation operation will suffer losses due to overlap loss (since the two chirps have slightly different frequency content), and correlation loss due to the different chirp-rates in the two signals. The resulting pulse compressed waveform has a reduced pulse compressed signal peak height, and a shift in the peak location. Since the temporal Doppler distortion is caused by the known platform-to-target geometry, this temporal distortion can be corrected for during processing. The compensation of temporal Doppler on chirps is analyzed shortly.

3. LINEAR FM AND HYPERBOLIC FM DOPPLER TOLERANCE

Analysis of the velocity and acceleration tolerance of LFM chirp signals and Hyperbolic FM (HFM) signals (signals with linear increasing or decreasing periods) is performed by analyzing *wideband ambiguity diagrams* [6–8, 10]. A wideband ambiguity surface is formed by correlating Doppler distorted versions of a pulse with its undistorted version. The decrease in the pulse compressed signal peak, and shift in the location of the signal peak then gives an idea of the Doppler tolerance of the waveform. The wideband ambiguity function in (19) is the correlation (pulse compression) of the Doppler distorted chirp with the undistorted chirp; for the LFM chirp

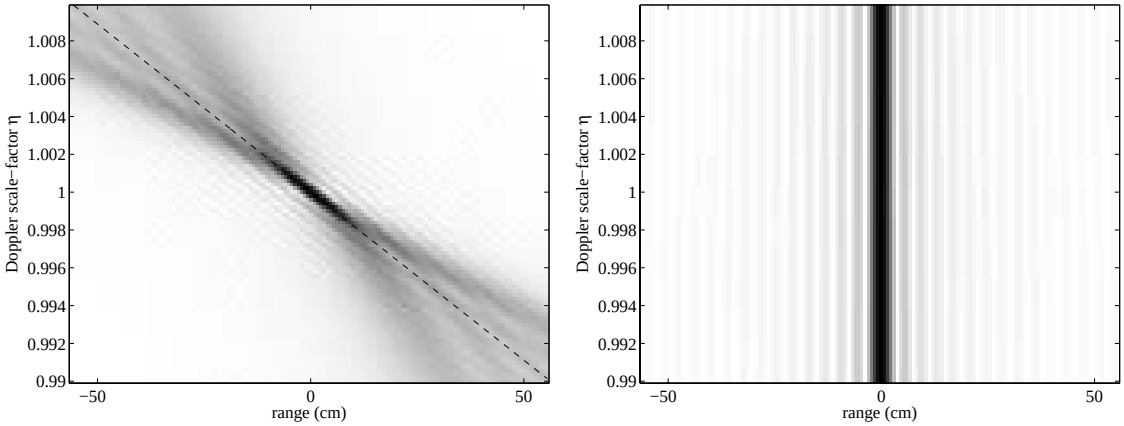

Figure 1: Wideband ambiguity functions. (a) Doppler distorted chirp pulse compressed with the nominal chirp, and (b) compensated for Doppler distortion.

this is (ignoring the amplitude factor dependent on η)

$$\begin{aligned}\chi_{\mathrm{lfm}}(\tau,\eta) &\approx \mathcal{F}^{-1}\left\{P\left(\frac{f}{\eta}\right)\cdot P^*(f)\right\} \approx \mathcal{F}^{-1}\left\{P\left(\frac{f}{\eta}\right)\cdot\sqrt{\frac{K}{j}}\cdot\exp\left(j\pi\frac{(f-f_0)^2}{K}\right)\right\} \\ &\approx \mathcal{F}^{-1}\left\{\mathrm{rect}\left(\frac{f-\eta f_0}{\eta B}\right)\cdot\exp\left(j\pi\frac{(\eta^2-1)f^2-2f_0\eta(\eta-1)f}{\eta^2 K}\right)\right\}\end{aligned} \tag{27}$$

where instead of pulse compressing with $P(f)$, we simply use the matching phase function (and cover enough bandwidth to enclose all possible Doppler shifts). From this analysis, it is clear that for $\eta \neq 1$ the pulse compression operation leaves residual quadratic and linear phase terms. The residual quadratic phase causes a loss of peak magnitude and peak broadening, while the residual linear phase causes a shift in peak location, i.e.,

$$\tau = -\frac{f_0\eta(\eta-1)}{\eta^2 K} = \frac{f_0(1/\eta-1)}{K} \tag{28}$$

where for $\eta = 1$, $\tau = 0$ so there is no error, for an approaching target $\eta > 1$, so $\tau < 0$, and for a receding target $\eta < 1$, so $\tau > 0$. The peak of the ambiguity function follows the line given by the peak shift equation when solved for η

$$\eta = \frac{1}{1+\frac{K\tau}{f_0}} \approx 1 - \frac{K\tau}{f_0} = 1 - \frac{B}{f_0\tau_p}\cdot\tau \tag{29}$$

which matches the results of Harris and Kramer [6,8] and others, but was derived in a different manner.

Figure 1(a) shows the wideband ambiguity diagram for an $f_0 = 30$kHz, $B = 20$kHz, $\tau_p = 50$ms LFM chirp signal. In Figure 1(a) we have plotted η against range-error $c\tau/2$ to more clearly show that the Doppler time-scaling causes a range error in the pulse compressed signal. Figure 1(a) is

plotted with a range span of thirty range resolution cells. Changing the transmitted pulse length, while keeping this range span fixed, produces an identical looking wideband ambiguity diagram, with a different Doppler scale-factor axis scaling. Wideband ambiguity analysis is typically used to determine the tolerance of waveforms used by a stationary source to track moving targets, in that case, the received waveform is analyzed to determine the target velocity. In the case of SAS, it is the platform movement that causes the waveform distortion, and this movement is known, as such, the SAS processor can correct for the known temporal Doppler distortion. Figure 1(b) emphasizes this fact by redrawing the wideband ambiguity surface with the Doppler distorted pulses pulse compressed using their known Doppler distortion.

The dispersion of the pulse compressed chirp peak in Figure 1(a) is the reason that the LFM chirp is not considered a Doppler tolerant waveform. The HFM waveform is considered a Doppler tolerant waveform [12], however, it should be noted that the peak of the wideband ambiguity surface for a HFM signal exhibits the *same* range change as the chirp signal as given by (29) [10], however, the magnitude of the HFM wideband ambiguity peak does not have the significant drop in that is seen for the LFM chirp. This means that a HFM signal can not be used in place of a LFM chirp to create a Doppler tolerant SAS. Systems using either form of transmitted signal still require Doppler compensation of the received data to achieve diffraction-limited resolution.

We can use the slope equation (29) to determine a criteria for ignoring temporal Doppler distortion. Using the same criteria as unfocused synthetic aperture processing, i.e., $\Delta r < \lambda_0/8$, we get the criteria for uncompensated Doppler processing; that is,

$$\Delta\eta < \frac{B}{4f_0^2\tau_p}. \tag{30}$$

Given an approximate Doppler scale factor of $\Delta\eta \approx 2\dot{r}/c \approx 2v_p \sin\theta(t)/c$ (where $\theta(t) \in [-\theta_B/2, \theta_B/2]$ is the angle to the target and v_p is the platform velocity in the along-track direction) we can determine an along-track velocity criteria based on the maximum Doppler shift at the edge of the beamwidth, i.e.,

$$v_p < \frac{c}{\theta_B} \cdot \frac{B}{4f_0^2\tau_p}. \tag{31}$$

The receivers on the Kiwi-SAS are constructed from 75mm PVDF tiles. Earlier designs used a single receiver three tiles long, i.e., $D = 225$mm, giving a $\theta_B \approx \lambda_0/D = 13^\circ$ beamwidth at 30kHz, while the more recent designs record data from the individual tiles, giving a 38° beamwidth. For a 225mm receiver, (31) gives the maximum along-track velocity below which Doppler can be ignored as is 0.75m/s for a 50ms chirp, and 0.19m/s for a 200ms chirp. For a 75mm receiver, the maximum velocities reduce to 0.25m/s and 0.06m/s.

The analysis of the effect of temporal Doppler shows that any SAS system with high along-track resolution (small receiver length) towed at a reasonable along-track speed (1m/s or more) will require temporal Doppler compensation. SAS temporal Doppler compensation can be applied in two ways. Raw data can be received and stored by the sonar in its uncompressed form in the (t, u)-domain, and then since the Doppler scale factor is dependent on angle, the pulse compression of the Doppler distorted chirp can be performed in the (ω, k_u)-domain. Alternatively, the data can be received and pulse compressed using the nominal LFM signal, and a then the phase-only Doppler compensator $DD(\omega, k_u)$ shown below can be applied during SAS image

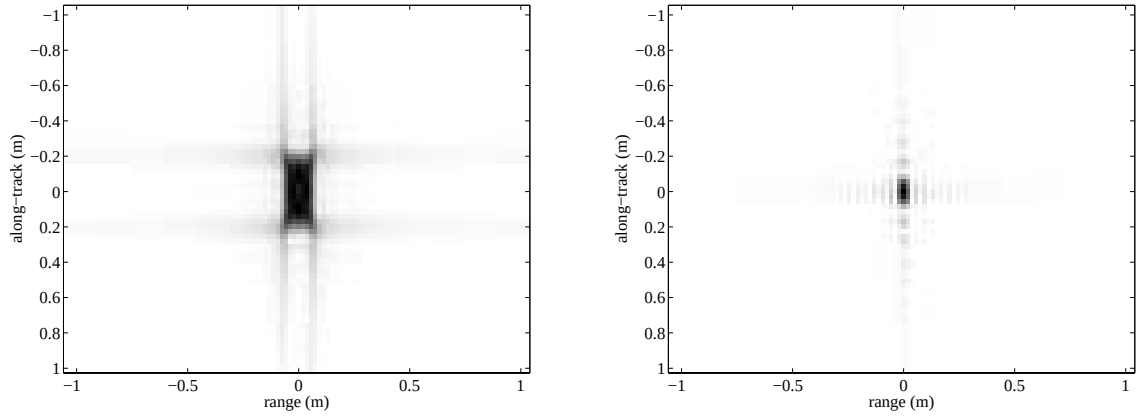

(a) (b)

Figure 2: Doppler compensated SAS processing. (a) focused image $\widetilde{ff}$ without LFM pulse Doppler compensation, (b) focused image ff with Doppler compensation.

reconstruction to remove the residual Doppler components.

$$DD(\omega, k_u) = \left\{ \exp\left(j\pi \frac{(f + f_0 - \eta f_0)^2}{\eta^2 K} \right) \cdot \exp\left(-j\pi \frac{f^2}{K} \right) \right\} \tag{32}$$

where $f = \omega/(2\pi)$, $f_0 = \omega_0/(2\pi)$, and the angular dependent η is

$$\eta \approx 1 - \frac{2\dot{r}(t)}{c} = 1 + \frac{2v \sin\theta}{c} = 1 + \frac{v}{c} \cdot \frac{k_u}{k}. \tag{33}$$

Equation 32 is applied to compensate for the Doppler effect within the transmitted LFM chirp. The motion of the platform also modifies the form of the target impulse response. Reference [1] provides details on the modifications required to the wavenumber algorithm to compensate for the effect of motion.

Figure 2 shows the effect of Doppler on the image processing of a single SAS target. The SAS imaging parameters are as per the Kiwi-SAS system; $f_0 = 30$kHz, $B = 20$kHz, $\tau_p = 200$ms, $D = 225$mm, and $v = 2$m/s. Equation 31 indicates a maximum speed without compensation of Doppler of 0.19m/s. At a velocity of 2m/s, to image a swath of say 200m width would require a repetition rate of approximately 267ms. The distance moved between pings would be 533mm, which exceeds the length D, indicating that multiple along-track receivers would be required to implement this example. For this simulation, the along-track dimension was adequately sampled without regard to how this was implemented. Since the image contains only a single-point target, it is sufficient to match filter the target without applying any further image correction, eg. in the wavenumber algorithm the final step involves an interpolation from the (ω, k_u)-domain onto the (k_x, k_y)-domain. Simulations using a multiple along-track receiver SAS simulator that does apply these steps shows similar results. The SAS processor for this simulation generates a pulse-compressed echo data set $\widetilde{ss}(t, u)$ (where pulse compression using the conjugate of the nominal LFM chirp was performed). Once Fourier transformed into the (ω, k_u) domain, $\widetilde{SS}(\omega, k_u)$ $(= \mathcal{F}\{\widetilde{ss}(t, u)\})$ is then modified by the Doppler compensator $DD(\omega, k_u)$, and a matched-filter MM based on the SAS system model that incorporates displacement of the

platform between transmission and reception (MM also includes amplitude compensation for k-dependent amplitude of the spectra). Figure 2(a) shows an image $\widetilde{ff}$ generated from the Fourier data $\widetilde{FF} = \widetilde{SS} \times MM$, i.e., the Doppler residuals in the chirp are not compensated, while Figure 2(b) shows an image ff generated from the Fourier data $FF = \widetilde{SS} \times DD \times MM$, i.e., the Doppler residuals in the chirp are compensated. If the stop-and-start model is used to generate MM, then there would also be a target location offset in the along-track dimension. No windowing was applied to the image spectral data, and the data was normalized using the calculated expected magnitude, eg., during processing the spectrum FF has unity magnitude, and the image ff is divided by $D/(2B)$ to normalize it. Simulations with smaller apertures, larger speeds, and for targets at various ranges gave similar results (the parameters above with a target at a range of 20m was chosen for fast simulation).

4. DOPPLER EFFECTS ON MICRONAVIGATION AND AUTOFOCUS

The effect of temporal Doppler on micronavigation techniques such as the displaced phase centre antennas DPCA algorithm (also called the residual phase centres RPC algorithm) is an unanswered question. We hope to answer this question when we complete the development of a SAS simulator that incorporates (among other features) Doppler signal distortion, target aspect dependence and target strength variability during raw data generation, and a SAS processor that incorporates DPCA and other autofocus algorithms during processing. With this in mind, we'll continue our discussion, presenting our thoughts on the possible effect of Doppler on image post-processing.

DPCA relies on the phase centre of a bistatic tx-rx pair for one ping to be in exactly the same position as a matching tx-rx pair from a subsequent ping [13]. Any time (or phase) difference between the two fast-time records is assumed to be due to a displacement error. So before this displacement error of the phase centre can be estimated, the fast-time data for each bistatic tx-rx pair needs to be individually corrected for angle of arrival as well as range as a function of separation.

For a moment let us ignore the temporal Doppler and deal only with the path length and subsequent phase errors due to the difference between bistatic and monostatic (phase centre) geometry. The difference between the bistatic geometry and the hypothetical monostatic geometry depends on the physical separation from the tx to any particular rx in the array as well as the distance moved between the instance of transmission and that of reception. The phase centre error (the path length difference between the bistatic tx-rx pair and a hypothetical monostatic tx-rx pair co-located at the phase centre halfway between the tx and rx) is worst at broadside and so it is common practice to correct for this path length error for a point reflector at the centre of the swath. This is known as the bulk phase centre error correction. The residual phase error for the corrected data is now zero at broadside for the swath centre and gets larger for increasing angles of arrival but also varies with range offset from the swath centre.

It is difficult to correct the phase centre error for all angles of arrival since the angular-dependent phase centre correction, even after bulk phase centre correction, is different for each tx- rx pair in the hydrophone array. To correct for all angles of arrival, it will be necessary to compute $sS_p(t, k_h) = \mathcal{F}_h\{ss_p(t, h)\}$ where p is the ping number, h the along-track offset of any specific hydrophone so k_h is directly proportional to angle of arrival, then filter out all but a single angle, inverse transform the filtered data back into the hydrophone domain to correct the fast time

data for each tx-rx pair and then repeat this for all angles within the beam. This processing overhead may be best done within any digital spotlighting process in which case all angles may not need to be corrected for each ping; just those angles that encompass the target of interest.

The variation of phase centre correction for range offset from the swath centre is probably best done by dividing the full swath width up into relatively narrow sub-swaths and then correcting each sub- swath independently with the appropriate sub-swath bulk phase centre error correction. This seems to be current practice anyway since it then becomes possible to ignore sections of the fast time data that have low cross correlation between two sequential pings. Unfortunately this narrow sub-swath approach will become increasingly questionable as transducer beamwidths get wider. Only after the phase centre error correction has been completed can it be determined whether the Doppler-induced residual phase error will be larger than the residual phase error of the phase centre corrected data.

To get a feel for the magnitude of the two contributions to the total phase error, take the example used in the previous section. At a range offset to the swath centre of 100m and a separation between the tx and rx of 0.226m (this includes the distance moved between transmission and reception for a target at 100m) the bulk phase centre correction is 0.016 of a wavelength. Subtracting this bulk phase centre error means that the residual phase centre error at $\pm 6.5^\circ$ from broadside is no more than -2.5×10^{-4} wavelengths or -1.6×10^{-3} rads of phase error at a range of 100m and no more than -1.3×10^{-2} rads at a range of 200m assuming the fast time data is bulk corrected for 100m. N.B. The longer range decreases the phase centre error but the greater separation between the positions of transmission and reception due to the longer range increases the phase centre error.

Now to the Doppler-induced phase error towards the beam edge at $\pm 6.5^\circ$ from broadside. For ping one, the total Doppler shift of the carrier frequency on the outward and return leg is 8.4254 Hz and for the same phase centre but now of ping two is 8.4255 Hz; a difference of 1.2×10^{-4} Hz. The extra Doppler-induced time delay in the cross-correlation of the outputs of the two phase centres is equivalent to $\pm 1.0 \times 10^{-4}$ rads at 30kHz; still only a fraction of the residual phase centre error at that same angle from broadside. Even at $\pm 20^\circ$ off broadside, the Doppler-induced phase shift in the cross-correlation is less than $\pm 3.0 \times 10^{-4}$ rads.

Autofocus techniques, such as the well-established phase gradient autofocus (PGA), are iterative algorithms that work on the reconstructed but distorted image $\widetilde{ff}$ [14]. However as a preprocessing and signal conditioning step, coarse motion compensation is usually applied to the raw data from the hydrophone receiver(s) using the navigational history from the INS and then perhaps fine motion-compensation using a micronavigation technique (such as DPCA) before the motion compensated data is used in the image reconstruction algorithm [15]. This results in the distorted image $\widetilde{ff}$. Autofocus techniques now try to focus this reconstructed but distorted image without further recourse to the flight path (navigation) history. So far these autofocus techniques have been most successful on a single receiver spotlight SAR where the entire object to be focussed has been distorted by the same point spread function. Since there are few real-time, transmit-beam spotlight SAS systems currently deployed, this would imply some post-detection digital spotlighting of strip map SAS raw data to produce data suitable for PGA and similar image domain algorithms.

However the spotlight process is implemented—whether real-time by beam steering the transmitter or post-detection on strip-map data, the important question, yet to be answered, is "Do

the phase errors induced by the uncorrected temporal Doppler in the reconstructed image prevent an autofocus algorithm converging to the correct solution?" A more pertinent question is "Do the residual phase errors in the corrected temporal Doppler data prevent an autofocus algorithm converging to the correct solution?" Now to answer the latter question, there may be a significant difference between a SAS using a single receiver and one using a multiple hydrophone array of receivers. With a single receiver SAS, no angular discrimination is possible for a single ping so some multi-ping processing (that cannot completely exclude the effect of sway errors) must be done before Doppler correction is possible. In contrast using a multiple hydrophone array of receivers, it is possible to perform Doppler correction ping by ping before the data is combined in the image reconstruction process thus avoiding any sway error complications in the Doppler compensation. Doppler effects increase with angle from broadside but for any specific angle, temporal Doppler effects are constant for all hydrophones and for all ranges so it is a relatively simple correction of the $sS_p(t, k_h)$ data for all $1 < p < P$ pings. Here we are making the assumption that any sonar platform yaw errors are a fraction of the transducers beamwidth as they would be for any well-controlled towfish or AUV. Since the operation of any true autofocus algorithm is very target dependent, it is quite uncertain at this early stage to know just how much uncorrected temporal Doppler can be tolerated before the algorithm no longer converges to the diffraction-limited image.

5. DISCUSSION AND CONCLUSIONS

All operational SAS systems experience some Doppler time scaling effects. However with the increasing use of higher speed, multiple receiver sonars, these systems should employ Doppler compensation within the image reconstruction algorithm to produce high-quality diffraction-limited images especially if accurate radiometric or target strength estimates are desired.

HFM is considered to be a Doppler tolerant waveform. However, this Doppler tolerance is in the context of target *detection* and not SAS imaging. Wideband ambiguity analysis of HFM signals show that the peak undergoes an identical range error shift as that of LFM. Hence in the context of SAS imaging, HFM is no better than LFM, both require Doppler compensation. The time-compression effects of Doppler would also need to be accounted for when performing SAS imaging using more 'covert' coded waveforms.

An additional argument for the use of Doppler compensation is that any residual phase errors due to uncompensated Doppler is likely to cause a bias in any autofocus algorithm especially if there is a strong aspect- dependent target in the field of view.

Autofocus algorithms often relate the residual phase in an image to some form of platform motion error, so the phase error due to temporal Doppler in the perfectly linear along-track motion case will produce a non-zero autofocus correction, i.e., the Doppler phase residuals can cause a target dependent bias in the autofocus estimate. How much phase error due to uncorrected Doppler (and also how much residual phase error after the Doppler has been corrected) can be tolerated and still have an autofocus algorithm converge is unknown at this stage since it is so target and target-aspect dependent.

Although incomplete Doppler correction may cause a phase (i.e., a timing) error in DPCA and similar micronavigation algorithms, the errors are still smaller than the residual phase centre errors after bulk phase centre correction and even after full angle of arrival correction. As longer arrays, wider swaths and higher tow speeds are employed, both the residual phase centre error

and the phase error due to temporal Doppler will increase but it is likely that the phase errors caused by incomplete phase centre error correction will always be greater than any phase errors caused by incomplete Doppler correction.

REFERENCES

[1] Hawkins DW. SAS Temporal Doppler. SAS Technical Report 001. Owens Valley Radio Observatory (OVRO), California Institute of Technology, 2004. (available at `http://www.ovro.caltech.edu/~dwh/sonar`)
[2] Rihaczek AW. *Principles of high resolution radar*. McGraw Hill, Inc, 1969.
[3] Woodward PM. *Probability and information theory, with applications to radar*. McGraw-Hill, New York, 1953.
[4] Mitchell RL and Rihaczek AW. Matched-filter responses of the linear FM waveform. *IEEE Transactions on Aerospace and Electronic Systems*, May 1968, 4(3) 417-432.
[5] Cook CE and Bernfeld M. *Radar signals: an introduction to theory and application*. Academic Press Inc., 1967.
[6] Harris B and Kramer SA. Asymptotic evaluation of the ambiguity functions of high-gain FM matched filter sonar systems. *Proc. IEEE* December 1968, 56(12):2149–2157,.
[7] Hermand J and Roderick WI. Delay-doppler resolution performance of large time-bandwidth-product linear FM signals in a multipath ocean environment. *Journal of the Acoustical Society of America*, November 1988, 84(5):1709–1727.
[8] Kramer SA. Doppler and acceleration tolerances of high-gain, wideband linear FM correlation sonars. *Proceedings of the IEEE*, May 1967, 55(5):627–636.
[9] Kelly EJ and Wishner RP. Matched-filter theory for high-velocity, accelerating targets. *IEEE Transactions on Military Electronics*, January 1965, 9:56–69.
[10] Lin Z. Wideband ambiguity function of broadband signals. *Journal of the Acoustical Society of America*, June 1988, 83(6):2108–2116.
[11] Kroszczynski JJ. Pulse compression by means of linear-period modulation. *Proceedings of the IEEE*, July 1969, 57(7):1260–66.
[12] Chatillon J, Bouhier ME and Zakharia ME. Synthetic aperture sonar for seabed imaging: relative merits of narrow-band and wide-band approaches. *IEEE Journal of Oceanic Engineering*, Jan. 1992, 17(1):95-105.
[13] Bellettini A. and Pinto MA. Theoretical accuracy of synthetic aperture sonar micronavigation using a displaced phase-center antenna. *IEEE Jour. Oceanic Eng.*, Oct. 2002, 27(4):780-789
[14] Jakowatz CV, Wahl DE, Eichel PH, Ghiglia DC and Thompson PA. *Spotlight-mode synthetic aperture radar: A signal processing approach*. Kluwer Acad., Boston, 1996.
[15] Hansen RE, Saebo TO, Gade K and Chapman S. Signal processing for AUV based interferometric synthetic aperture sonar. *IEEE OCEANS Proc.*, Sept. 2003, 1:2438-2444.